A simple and effective method for quantifying spatial anisotropy of time series of precipitation fields

Tero J. Niemi[1], Teemu Kokkonen[1], and Alan W. Seed[2]

[1]Department of Civil and Environmental Engineering, School of Engineering, Aalto University, Espoo, Finland, [2]Centre for Australian Weather and Climate Research, Bureau of Meteorology, Melbourne, Victoria, Australia

Abstract The spatial shape of a precipitation event has an important role in determining the catchment's hydrological response to a storm. To be able to generate stochastic design storms with a realistic spatial structure, the anisotropy of the storm has to be quantified. In this paper, a method is proposed to estimate the anisotropy of precipitation fields, using the concept of linear Generalized Scale Invariance (GSI). The proposed method is based on identifying the values of GSI parameters that best describe isolines of constant power on the two-dimensional power spectrum of the fields. The method is evaluated using two sets of simulated fields with known anisotropy and a measured precipitation event with an unknown anisotropy from Brisbane, Australia. It is capable of accurately estimating the anisotropy parameters of simulated nonzero fields, whereas introducing the rain-no rain intermittency alters the power spectra of the fields and slightly reduces the accuracy of the parameter estimates. The parameters estimated for the measured event correspond well with the visual observations on the spatial structure of the fields. The method requires minimum amount of decision making and user interaction, making it suitable for analyzing anisotropy of storm events consisting of long time series of fields with a changing spatial structure.

1. Introduction

Rainfall is needed as input for rainfall-runoff models that are used in hydrological design studies, for example, to size hydraulic structures such as spillways and culverts or to test the performance of a storm sewer network under extreme conditions. The design storm can be based on an observed rainfall event, or it can be based on the spatial and temporal statistical structure of a rainfall event with a given duration and an average recurrence interval. The hydrological response of a catchment to rainfall has been found to depend on the spatial and temporal structure of the rainfall, particularly at the urban scale [*Segond et al.*, 2007]. Multifractal models, such as those based on multiplicative cascades [e.g., *Gupta and Waymire*, 1993; *Seed et al.*, 1999; *Kang and Ramírez*, 2010; *Gires et al.*, 2012] or nonlinear filtering of correlated Gaussian noise [e.g., *Pegram and Clothier*, 2001; *Rebora et al.*, 2006; *Paschalis et al.*, 2013], have proven to be useful in creating stochastic rainfall fields with correct spatial statistics, and have been used to generate ensembles of high-resolution rainfall fields in space and time for hydraulic design [*Seed et al.*, 2002]. These models assume, however, that the rainfall structures are isotropic. In reality, the fields are rarely isotropic, but often consist of bands of rainfall that are associated, e.g., with synoptic cold fronts or mesoscale squall lines [*Houze and Hobbs*, 1982; *Rauber and Ramamurthy*, 2003].

Being able to simulate fields with a correct anisotropic structure is important, since the catchment's response to a storm may be very different depending on the shape and movement of the storm. For example, consider a long and narrow band of high-intensity rainfall moving over an urban catchment. A storm moving in the direction of its elongation will produce large rainfall accumulations over a small area, and is more likely to cause flooding than a storm that moves perpendicular to its elongation resulting in the rainfall being distributed over a larger area [*Doswell et al.*, 1996]. An example of an anisotropic rainfall event is presented in Figure 1, where a significant storm moved over Brisbane, Australia, on 10 January 2011 along the orientation of its rainband producing over 50 mm of accumulated rain in just 1 h. *Brauer et al.* [2011] present another example from the Netherlands, where a mesoscale squall line storm resulted in 24 h rainfall accumulations of 160 mm exceeding the return period of 1000 years. The capacity to stochastically generate such events requires a methodology to identify and describe the anisotropy present in precipitation patterns.
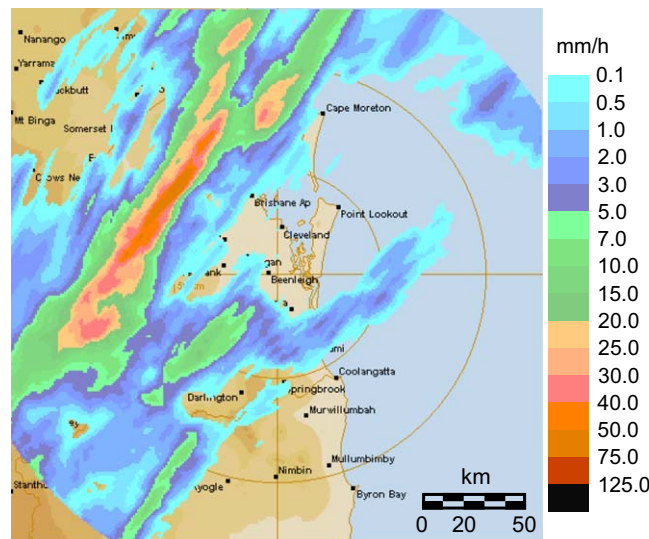
Figure 1. An example of a strongly anisotropic significant rainfall event in Brisbane, Australia, on 10 January 2011. The storm was moving along the orientation of the rainband resulting in an hourly rainfall accumulation exceeding 50 mm between 21:00 and 22:00 UTC.

Two-dimensional autocorrelation functions are a common tool to study anisotropy of geophysical fields, since they allow one to analyze both the scale over which patterns occur and the direction of the pattern. Therefore, they have been extensively used to study the highly varying spatial structure of precipitation fields [e.g., *Zawadzki*, 1973; *Baldwin et al.*, 2005; *Velasco-Forero et al.*, 2009; *Ebtehaj and Foufoula-Georgiou*, 2010; *Mandapaka and Qin*, 2013].

The autocorrelation is directly related to the Fourier power spectrum through the Wiener-Khinchin theorem, which states that the autocorrelation $C(\tau)$ of a function $R(\boldsymbol{x})$ is an inverse Fourier transform of the power spectrum $P(\boldsymbol{k})$ of the same function:

$$C(\tau) = \mathcal{F}^{-1}(P(\boldsymbol{k})) \tag{1}$$

where $\boldsymbol{k} = (k_x, k_y)$ is the wave number in the Fourier domain corresponding to location $\boldsymbol{x} = (x, y)$ in the spatial domain, $\tau = (\tau_x, \tau_y)$ describes the lag, and $\mathcal{F}$ denotes the Fourier transform operation. Using the power spectrum provides practical advantages when dealing with fields measured on a regular grid, such as radar precipitation fields in this paper, since it can be easily computed using standard two-dimensional fast Fourier transform (FFT) algorithms [e.g., *Press et al.*, 2007] as the square modulus of the Fourier transform $F(\boldsymbol{k})$ of the original field $R(\boldsymbol{x})$:

$$P(\boldsymbol{k}) = |F(\boldsymbol{k})|^2 \tag{2}$$

The two-dimensional power spectrum is usually radially averaged using circles centered at $k_x = k_y = 0$, yielding what is referred to here as an isotropic energy spectrum $E(k)$, where $k = |\boldsymbol{k}| = \sqrt{k_x^2 + k_y^2}$. The term isotropic implies here that averaging around $k_x = k_y = 0$ integrates out the potential anisotropy in the spectrum making it easier to study the spatial structure of the field.

The isotropic energy spectrum is commonly used to evaluate the scaling structure of the field since the necessary condition for scale invariance is that the spectrum of the field must follow:

$$E(k) \sim k^{-\beta} \tag{3}$$

where the spectral exponent β is an indicator of scaling, or smoothness, of the field [*Menabde et al.*, 1997]. Isotropic scaling of precipitation fields according to equation (3) has been reported in a number of earlier studies [e.g., *Nykanen and Harris*, 2003; *Mandapaka et al.*, 2009; *Rysman et al.*, 2013; *Seed et al.*, 2013].

Quantifying anisotropic scaling of geophysical fields by using different spectral exponents for different directions has been suggested by several authors [e.g., *Fox and Hayes*, 1985; *VanZandt et al.*, 1990; *Pilkington and Todoeschuck*, 1993; *De Michele and Bernardara*, 2005; *Ebtehaj and Foufoula-Georgiou*, 2011]. These methods suffer, however, from not being able to parameterize the scaling in different directions unambiguously, which is required for a straightforward implementation into a simulation model. Also, rather than being

independent of a specific scale, which is the very requirement for a system being scaling, these methods are dependent on the size of the structures [*Lewis et al.*, 1999].

Generalized Scale Invariance (GSI) was introduced by *Lovejoy and Schertzer* [1985] as a general formalism to describe anisotropic scaling of multifractal fields of atmospheric turbulence. GSI provides an attractive option to quantify the scaling of anisotropic systems, since its linear approximation depends only on a few parameters that define the transformation from an isotropic to an anisotropic system. The first attempt to determine the GSI parameters of geophysical fields was the "Monte Carlo differential rotation" technique [*Pflug et al.*, 1993]. *Lewis et al.* [1999] criticized this method for giving biased estimates of the anisotropy parameters and suggested an improved "Scale invariant generator" (SIG) technique. *Beaulieu et al.* [2007] reported that while SIG yielded reasonable estimates for theoretical simulations with a diversity of anisotropic and statistical characteristics, it was not able to quantify the true anisotropy of many empirical fields. Consequently, they proposed a new "Differential anisotropy scaling" technique.

The previously proposed methods to quantify anisotropy of geophysical fields through the use of GSI were developed for individual fields and they require some user intervention as well as subjective decision making. This complicates the application of these methods to a time series of rain fields where the anisotropy is expected to change during the event. In this paper, a method is proposed to estimate the GSI parameters for a continuously evolving anisotropy in a time series of precipitation fields. The proposed method aims to be fast and it requires a minimum amount of user intervention, in order to efficiently quantify the changing anisotropy throughout the duration of a storm event.

We are focusing on quantifying anisotropy in a multifractal framework using the GSI formalism due to its explicit description of the scaling behavior in precipitation fields. Nevertheless, other methods to assess anisotropy have also been proposed, and especially the methods based on geostatistics have been extensively used both for quantifying [e.g., *Miniscloux et al.*, 2001; *Ali et al.*, 2005; *Berne et al.*, 2009; *Kirstetter et al.*, 2010] and simulating [e.g., *Schleiss et al.*, 2009, 2012, 2014; *Vischel et al.*, 2009; *Leblois and Creutin*, 2013] the anisotropy encountered in precipitation fields. Alternatively, *Kumar and Foufoula-Georgiou* [1993a] and *Kumar* [1995] have also proposed wavelets for identifying the scale-space anisotropy in precipitation fields.

This paper is organized as follows. Section 2 provides a brief summary of the GSI formalism, outlines the new method to quantify anisotropic scaling, and presents a simple method to generate stochastic anisotropic fields. In section 3, the proposed method is applied to both simulated and measured precipitation fields and the results are presented. Discussion of the performance, assumptions, and practical limitations of the proposed method can be found in section 4, and finally some conclusions are drawn and further research suggested in section 5.

2. Methods

2.1. Generalized Scale Invariance

Isotropic scaling, as depicted by equation (3), implies that the (statistical) properties of a field at different scales are simply magnified (or reduced) versions of each other by some power of the scale ratio λ relating the scales. However, for anisotropic scaling systems, simple magnification (or reduction) is not sufficient but it must be accompanied by compression and/or rotation, both of which are functions of only the scale ratio λ. GSI was developed to address scaling in anisotropic systems and it states the most general conditions under which a system can be considered as scale invariant.

Following *Schertzer and Lovejoy* [1985] and *Lovejoy and Schertzer* [1985], three elements are required to completely define GSI. The scale changing operator T_λ, which transforms the scale of vectors by the scale ratio λ, may be written as:

$$T_\lambda = \lambda^{-\mathbf{G}} \tag{4}$$

where $\mathbf{G}$ is the generator defining the scale transformations (the anisotropy). Next, the unit scale ($\lambda = 1$) and the corresponding unit "ball" B_1 are defined. In general, B_1 defines all the unit scale vectors $\mathbf{k}_1$, and it can be used to generate all other nonunit scales and scale vectors $\mathbf{k}_\lambda$ by applying T_λ to B_1, i.e., $B_\lambda = T_\lambda B_1$. The choice of the unit ball B_1 can be arbitrary, but it is often convenient to select the scale where the system can be

considered isotropic for defining the unit ball (i.e., a circle in 2-D or a sphere in 3-D). Then the unit ball can be expressed using only one parameter, l_s, referred to as the "sphero scale." The last element required to define GSI is some measure of scale. For GSI in two dimensions, it is convenient to select this measure as the square root of the area of the ball B_λ [*Lewis et al.*, 1999].

Assuming statistical homogeneity of the fields, T_λ will be independent of the location in the field allowing the linear Generalized Scale Invariance [*Schertzer and Lovejoy*, 1985; *Lovejoy and Schertzer*, 1985] to be used. Although the assumption of homogeneity of the fields can be overly restrictive, it is usually possible to consider at least subregions of the field where the linear GSI assumption holds. In the linear GSI in two dimensions **G** is a 2×2 matrix, and can be written as a linear combination of quaternions represented as two-dimensional matrices:

$$\mathbf{G}=d\mathbf{1}+c\mathbf{K}+f\mathbf{J}+e\mathbf{I} \tag{5}$$

where:

$$\mathbf{1}=\begin{pmatrix} 1 & 0 \\ 0 & 1 \end{pmatrix}, \mathbf{K}=\begin{pmatrix} 1 & 0 \\ 0 & -1 \end{pmatrix}, \mathbf{J}=\begin{pmatrix} 0 & 1 \\ 1 & 0 \end{pmatrix}, \mathbf{I}=\begin{pmatrix} 0 & -1 \\ 1 & 0 \end{pmatrix} \tag{6}$$

Thus:

$$\mathbf{G}=\begin{pmatrix} d+c & f-e \\ f+e & d-c \end{pmatrix} \tag{7}$$

and using the series expansion of the exponential function, writing $a^2=c^2+f^2-e^2$, and defining $U=\ln\lambda$, we get from equation (4) [*Pflug et al.*, 1993]:

$$T_\lambda=\lambda^{-\mathbf{G}}=\lambda^{-d}\left[\mathbf{1}\cosh(aU)-(\mathbf{G}-d\mathbf{1})\frac{\sinh(aU)}{a}\right] \tag{8}$$

The components of **G** can be interpreted so that c and f are associated with stratification, e with rotation, and d with overall contraction of the system. The relative dominance of these operations can be distinguished by the sign of a^2. When $a^2>0$, the stratification of the system is dominant, whereas when $a^2<0$, the rotation dominates. Note that when $a^2<0$, the above equation holds, but a must be replaced with $|a|$ and hyperbolic trigonometric functions with their ordinary counterparts [*Pecknold et al.*, 1993]. Using the square root of the area of the ball as a measure of scale corresponds to $d=1$ [*Lewis et al.*, 1999].

2.2. Parameterization Method

In the method proposed here, l_s and the components of $\mathbf{G}=\mathbf{G}(c,e,f)$ (as by convention $d=1$) are estimated using the two-dimensional power spectrum of the precipitation fields. However, since the fields can be considered as realizations of a stochastic process, the scaling is not expected to hold exactly for any individual field but only for an ensemble average of fields produced using the same generator and the same sphero scale. Moreover, precipitation fields change constantly over time (nonstationarity), which causes **G** and l_s to vary from field to field. However, as the anisotropy of the field is typically caused by mesoscale structures, which evolve slowly in time relative to the smaller-scale features [*Germann and Zawadzki*, 2002; *Radhakrishna et al.*, 2012], the sampling rate of the radar (here 6 min) is assumed to be much faster than the rate of change in the spatial structure of the field (several hours). Therefore, it is assumed that the change in **G** and l_s is sufficiently slow so that a centered moving average of N fields (here over a time period of an hour) can be used to produce an ensemble average power spectrum $P_{avg}(\boldsymbol{k})$. This will then be used as the measure of scaling for each field at time t instead of the spectrum $P(\boldsymbol{k})$ of a single field. Furthermore, it is assumed that there exists a sphero scale, l_s, and this is used as the unit scale λ_1. Other functions could be used to describe the unit scale (see, e.g., *Lewis* [1993] for an example of a fourth-order equation describing the unit scale), but they would make the parameterization more complicated and increase the dimensionality of the problem. Sphero scale is assumed here for simplicity and due to the empirical observation that rain structures tend to become more isotropic at the small scale.
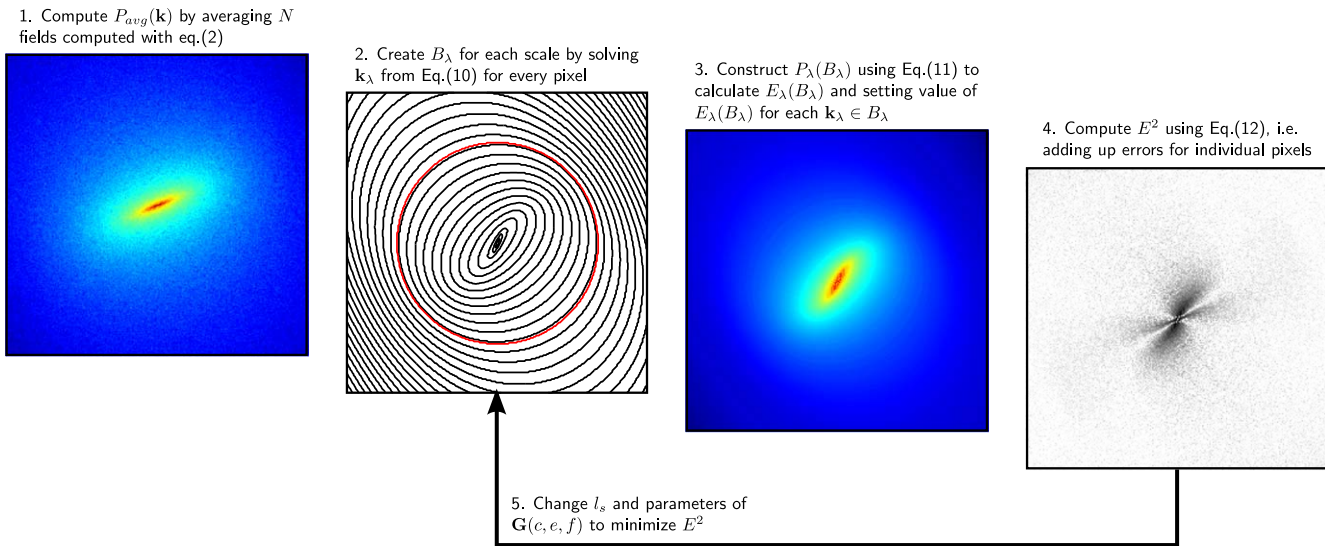
1. Compute $P_{avg}(\mathbf{k})$ by averaging N fields computed with eq.(2)

2. Create B_λ for each scale by solving $\mathbf{k}_\lambda$ from Eq.(10) for every pixel

3. Construct $P_\lambda(B_\lambda)$ using Eq.(11) to calculate $E_\lambda(B_\lambda)$ and setting value of $E_\lambda(B_\lambda)$ for each $\mathbf{k}_\lambda \in B_\lambda$

4. Compute E^2 using Eq.(12), i.e. adding up errors for individual pixels

5. Change l_s and parameters of $\mathbf{G}(c, e, f)$ to minimize E^2

Figure 2. The process for quantifying the anisotropy of an individual field. See details in text.

The method proposed here is based on finding isolines of constant power on $P_{avg}(\boldsymbol{k})$, representing structures of the same scale. It relies on the assumption that the isoline at scale λ is represented by the ball $B_\lambda = B_\lambda(\mathbf{G}, l_s) = B_\lambda(c, e, f, l_s)$ when the parameters describing $\mathbf{G} = \mathbf{G}(c, e, f)$ and l_s have correct values. As B_λ refers to all scale vectors of scale λ (i.e., $\boldsymbol{k}_\lambda$) in the anisotropic system, this is analogous to wavelengths k describing contours of constant power $E(k)$ in the isotropic case. Hence, the value confined by each B_λ can be seen as the "anisotropic wavelength" and is here referred to as k_λ. Graphical illustration of the method is presented in Figure 2.

Given a generator $\mathbf{G}$ and sphero scale l_s, $\boldsymbol{k}_\lambda$ can be solved from the equation:

$$\boldsymbol{k}_\lambda = \tilde{T}_\lambda \boldsymbol{k}_1 \tag{9}$$

where $\tilde{T}_\lambda = \lambda^{-\bar{\mathbf{G}}} = \lambda^{-\mathbf{G}^\mathsf{T}}$ is the Fourier space scaling operator corresponding to T_λ [*Pflug et al.*, 1993], and $\boldsymbol{k}_1$ is on the unit circle corresponding to the unit scale λ_1. In practice, equations (8) and (9) yield the following transcendental equation [*Pecknold et al.*, 1993] that has to be solved for each coordinate pair (k_x, k_y) to get k_λ for that location:

$$\ln\left(Q\cosh^2(a(U - U_1)) + R\sinh^2(a(U - U_1)) - S\sinh(2a(U - U_1))\right) = 2U$$

$$Q = k_x^2 + k_y^2$$

$$R = \frac{k_x^2\left(c^2 + (f - e)^2\right) + k_y^2\left(c^2 + (f + e)^2\right) + 4k_x k_y ce}{a^2} \tag{10}$$

$$S = \frac{\left(k_x^2 - k_y^2\right)c + 2k_x k_y f}{a}$$

$$U = \ln k_\lambda$$

where $U_1 = \ln k_1$ and the value of k_λ at (k_x, k_y) is simply $\exp(U)$. Finally, the value of each k_λ is rounded to the nearest integral value in order to have an integer field where each unique value represents a single B_λ.

Assuming that each B_λ should consist of $\boldsymbol{k}_\lambda$ describing an isoline on $P_{avg}(\boldsymbol{k})$, the "anisotropic energy spectrum" $E_\lambda(B_\lambda) = E_\lambda(c, e, f, l_s)$ is calculated in a similar manner as the isotropic energy spectrum $E(k)$:

$$E_\lambda(B_\lambda) = \frac{1}{n}\sum_{i=1}^{n}\left\{P_{avg}(i) \,|\, i \in B_\lambda\right\} \tag{11}$$

where index i refers to the location (k_x, k_y).

NIEMI ET AL.   5910

Finally, a candidate spectrum $P_\lambda = P_\lambda(B_\lambda) = P_\lambda(c, e, f, l_s)$ is constructed by assigning the respective average values of $E_\lambda(B_\lambda)$ to every location $\boldsymbol{k}_\lambda$. In other words, a field is created where each location (k_x, k_y) has a value from $E_\lambda(B_\lambda)$ determined by the value of k_λ at that location.

By comparing P_λ to P_{avg} pixel by pixel, $\mathbf{G}$ and l_s are estimated by minimizing the following error function $E^2 = E^2(c, e, f, l_s)$ (not to be confused with energy spectrum $E(k)$):

$$E^2(c, e, f, l_s) = \sum \frac{1}{k} \left[10 \log_{10} P_{avg}(\boldsymbol{k}) - 10 \log_{10} P_\lambda(\boldsymbol{k}) \right]^2 \tag{12}$$

The sum is over all the pixels in the spectra. Inverse distance weighting (IDW) is used to compensate for the undersampling at the large wave numbers and possible biases at the small wave numbers. IDW is chosen over anisotropic weighting according to k_{λ}, as using weighting that is based on B_λ would lead to different weights depending on the values of $\mathbf{G}$ and l_s that are to be estimated. This would complicate comparison of error function values for different $\mathbf{G}$ and l_s. Decibel units are used to reduce the large variability in the power spectrum values between high and low wave numbers. Finally, squaring the error function penalizes the large errors.

Identifying the minimum of E^2 can be implemented using any standard optimization algorithm that does not require derivatives of the error function. Here the classical downhill simplex method of *Nelder and Mead* [1965] is used to find the minimum of E^2. Since the parameterization problem is four dimensional, the simplex will consist of five vertices. Throughout the optimization, the initial simplex for each field is constructed by setting one vertex to the minimum of the previous field, and choosing the values of the remaining four vertices from uniform distributions. This is based on the assumption that parameters for consecutive fields are likely to be relatively close to each other. For the first field of the time series, all vertices are selected from uniform distributions, since there is no previous optimum to be used as one of the vertices. In an attempt to prevent the downhill simplex from finding only a local minimum, the optimization routine is restarted until the absolute difference in the values of E^2 between the current and previous iteration rounds is less than a predefined threshold or the maximum number of restarts is achieved.

The assumption of the linear GSI with the existence of a sphero scale places the following constraint on parameters c and f [*Schertzer and Lovejoy*, 1985]:

$$d^2 > c^2 + f^2 \tag{13}$$

Since d was set to $d = 1$, parameters c and f must now lie between -1 and 1. For parameter e, there is no such a simple constraint, but for practical reasons the parameter space for e has to be limited. *Lewis* [1993] suggests using limits of $[-1.5, 1.5]$ for e based on experience with analyzed geophysical fields. Although he analyzed satellite cloud radiance and sea ice SAR fields, these limits were adopted here for precipitation fields as well. The sphero scale, l_s, (in real-space units) is restricted by the Fourier transform to lie between twice the pixel size and the side length of the studied fields, i.e., in this study between 2 and 256 km.

2.3. Generating Stochastic Anisotropic Fields

The method adopted here to generate random fields with a given spatial scaling is a modified version of power law filtering Gaussian noise presented by *Bell* [1987] and *Schertzer and Lovejoy* [1987]. The former used this technique to simulate rain fields in three dimensions as seen by a satellite, and the latter applied it to simulate radar data. In this paper, realistic realizations of radar reflectivity (dBZ) fields are generated. Fields of reflectivity (dBZ) rather than rainfall rate (mm/h) are generated since measured reflectivity fields approximately follow truncated Gaussian distribution. Also, reflectivity fields can be transformed to rainfall rates using any standard R-Z relationship if needed.

A field of Gaussian white noise has no spatial structure, i.e., it has a flat power spectrum with $\beta = 0$ in equation (3). A white noise field can, however, be transformed to have a spatial correlation structure by filtering it in Fourier space using a power law filter with the desired β. Isotropic, as well as anisotropic, power law filters are defined as distance functions that decay as a power law (with an exponent of $-\beta/2$) from the

NIEMI ET AL.   5911

smallest frequency to the Nyquist frequency, and are then reflected around that point. The isotropic filter is described by:

$$H(\boldsymbol{k}) = k^{-\beta/2} \qquad (14)$$

For the anisotropic filter, wave numbers $\boldsymbol{k}$ have to be replaced by corresponding values of $\boldsymbol{k}_\lambda$ calculated with equation (10).

Following *Pegram and Clothier* [2001], four parameters were used to create realistic reflectivity fields: μ and σ, the mean and standard deviation of the reflectivity fields; *WAR*, the wetted area ratio (proportion of rainy cells to the total number of cells, in this case the fraction of the field with dBZ $>$ 10); and β, the spatial scaling parameter.

It should be noted that *WAR* here is not strictly a measure of rain-to-no-rain ratio, but rather a ratio between detectable and nondetectable signals of radar reflectivities. Rainfall echoes that are below 10–15 dBZ are difficult to separate from clear-air returns from, e.g., birds and insects. Setting a threshold for a detectable signal to 10 dBZ corresponds to the rain rate of 0.15 mm/h using the standard Marshall-Palmer distribution [*Marshall and Palmer*, 1948], so in any case only very small rainfall intensities are neglected.

The procedure to create random fields with given spatial statistics is described as follows:

1. generate a field of Gaussian white noise;

2. transform the field into Fourier space;

3. filter the field with a power law filter with the desired β;

4. inverse transform the field back to real space;

5. threshold the spatially correlated field to obtain the correct value of *WAR* (by setting values less than some threshold to zero); and finally

6. scale and shift the field by the given values of μ and σ.

Since thresholding is followed by scaling and shifting, the resulting field will have residual nonzero values where there should be no rain. These values have to be removed by forcing them to zero, i.e., by thresholding the field again by, e.g., setting values $<$10 dBZ to zero. This operation will slightly alter μ and σ of the field, but reversing the order of the operations would result in much inferior statistics.

3. Results

The performance of the proposed method was evaluated using both simulations with a known anisotropy and a measured precipitation event with an unknown anisotropy. Two sets of simulations were performed using the procedure described in section 2.3. Each simulation consisted of a series of random fields with 256 $\times$ 256 pixels. The statistics describing the fields were held constant throughout the simulations at $\mu=9.3$ dBZ, $\sigma=11.7$ dB, and $\beta=2.67$. For the second set of simulations, *WAR* was given a value of 0.38. These are the average statistics of the measured event studied in this paper. Anisotropy was introduced by changing l_s and the parameters of **G**. The simulations begin from an isotropic case and then anisotropy is introduced gradually by first changing one parameter at a time. After each parameter has been altered from the initial value, all parameters are changed simultaneously. Finally, parameters e and l_s are changed individually one more time. All the parameter changes are executed during 10 consecutive fields, and after each change, the parameter values are held constant for the next 10 consecutive fields. The selected time series was chosen to observe how altering parameters one by one and at the same time affects the performance of the parameterization method in a wide variety of anisotropic situations rather than trying to replicate some distinct physical situations. There is no temporal correlation between the generated fields, but the fields are a series of independent realizations of a stochastic process. For convenience, however, the sequence of simulated fields is also referred to as a time series to unify the language when describing the results of simulated and measured reflectivity fields.

3.1. Nonzero Random Fields
In the first set of simulations, nonzero random fields were generated by removing Step (5) from the procedure presented in section 2.3. The resulting fields have nonzero values in all pixels representing ideal
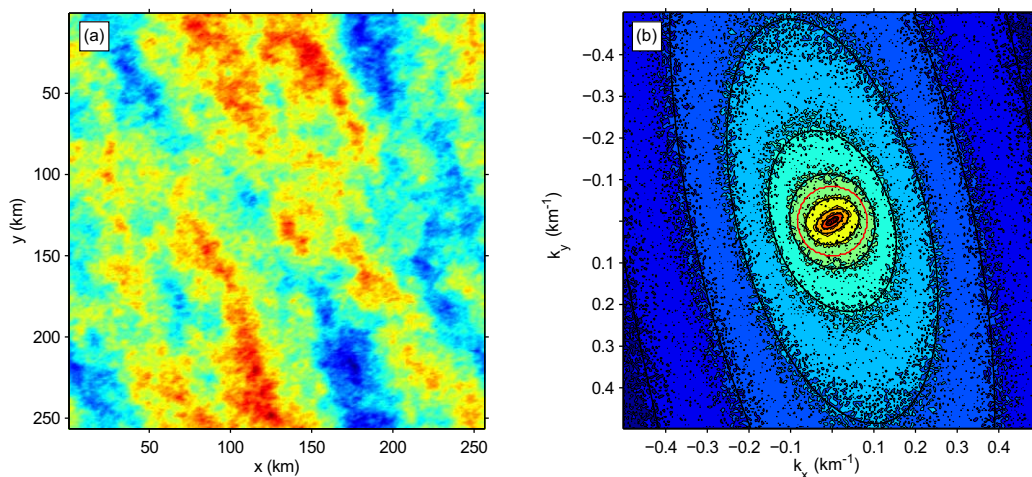
Figure 3. (a) An example of a nonzero random field, generated with $\mathbf{G}=\mathbf{G}(-0.2,-0.2,0.2)$ and $l_s=12$ km. (b) P_{avg} corresponding to the real-space field on the left with selected B_λ (black ellipses) produced with estimated generator parameters $\mathbf{G}=\mathbf{G}(-0.203,-0.200,0.204)$ and $l_s=12.07$ km (red circle). If $\mathbf{G}$ and l_s are correct, B_λ should describe isolines on P_{avg}.

conditions for the proposed parameterization method as no information on the spatial structure of the fields is lost through neglecting values less than a given threshold.

P_{avg} for each field was constructed by using a centered moving average of seven contiguous fields. Due to possibly large errors in power spectrum values computed for the smallest wave numbers, the 3 by 3 pixel area in the middle of the spectrum image was disregarded from the computation of the error function. An example of an anisotropic nonzero random field and the corresponding P_{avg} with estimated B_λ are presented in Figure 3. Note that due to the properties of the Fourier transform the orientation of the features in real space is orthogonal to the orientation in power spectrum. To evaluate the reliability of the proposed method, the parameterization procedure was repeated 15 times, and the average values and 95% confidence intervals for each parameter and for each time step were calculated (Figure 4). To better visualize variance and bias in the parameter estimates, Figure 5 shows scatterplots of estimated parameter values against the expected (i.e., input) values from the 15 replicates per time step.

3.2. Simulated Radar Reflectivity Fields
To evaluate the performance of the proposed parameterization method with realistic fields, yet knowing the true anisotropy, a set of simulated reflectivity fields was generat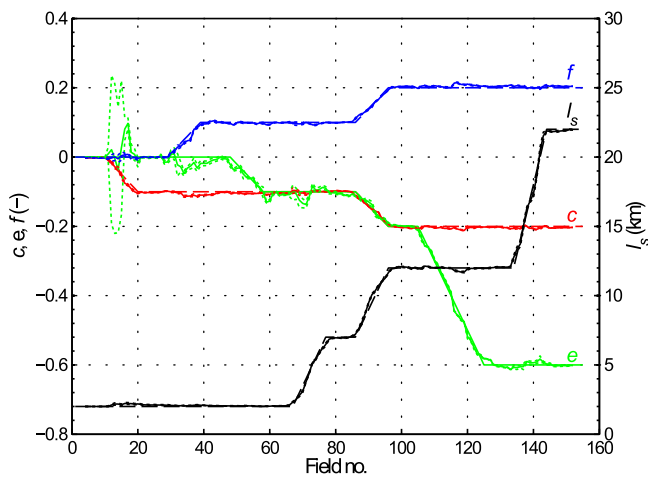ed using the same random generator seed and the same anisotropy as in section 3.1 (nonzero fields). However, to create intermittency similar to real reflectivity fields, the procedure outlined in section 2.3, including Step (5) of thresholding the fields, was followed. In addition, the noise fields were padded with zeros before the Fourier transform at Step (2) and returned back to the original size before Step (5) to prevent the unnatural wrap-around effect. Data windowing with a rotationally symmetric boxcar window, i.e., by setting values outside a radius of 128 pixels from the center of the field to zero, were used to alleviate the effects of spectrum corruption due to the discontinuities at the edges of the
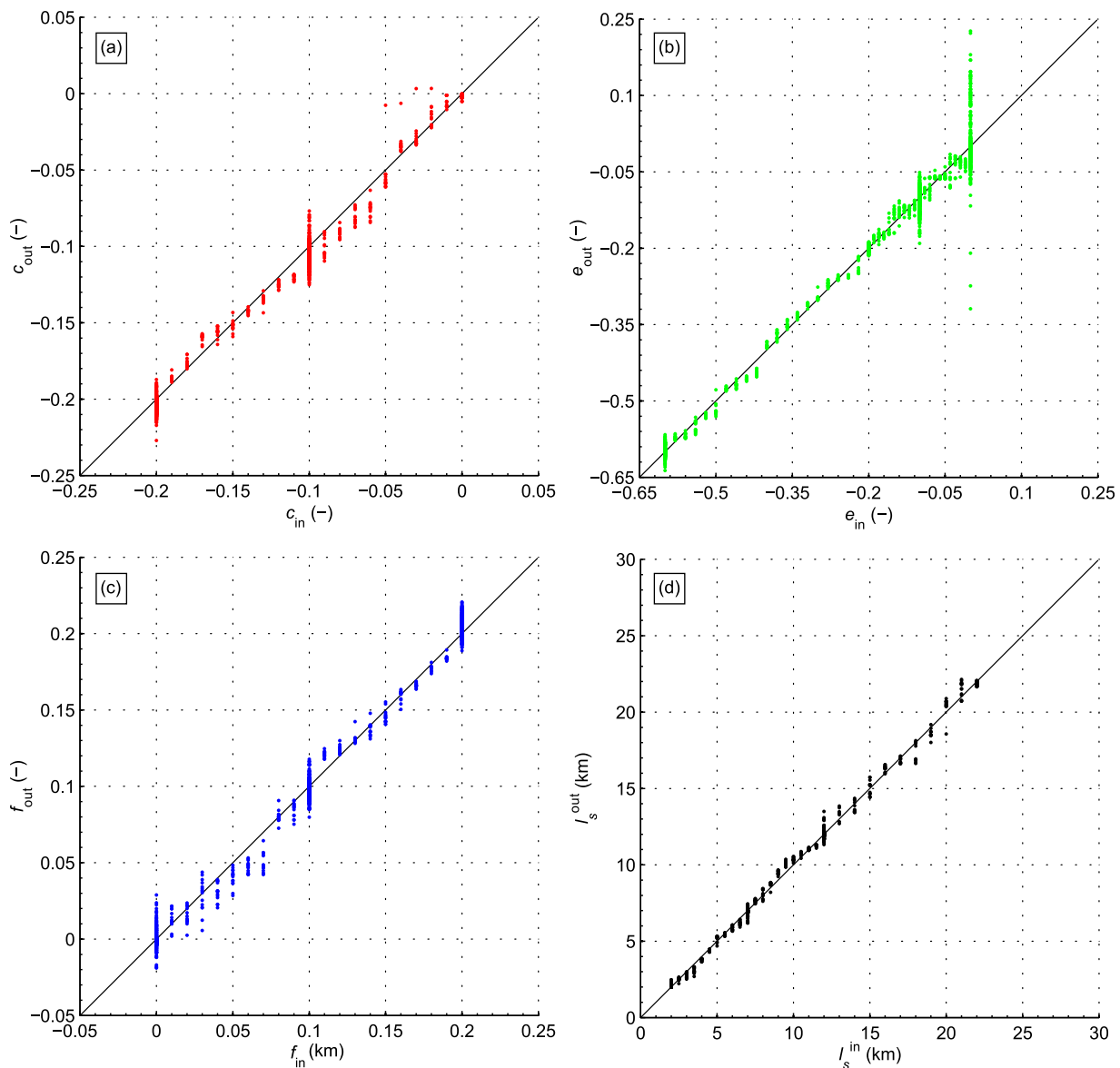

Figure 4. Average values (solid lines) and 95% confidence limits (dotted lines) of estimated anisotropy parameters for 15 parameterization rounds using nonzero random fields with gradually changing anisotropy. Dashed lines indicate input parameters. c—red, e—green, f—blue, and l_s—black.

Figure 5. Relationship between input (horizontal axis) and estimated (vertical axis) anisotropy parameters for 15 parameterization rounds using nonzero random fields. (a) c, (b) e, (c) f, and (d) l_s. Note that scale for e_{out} is truncated due to the large variance at $e_{in} = 0$.

image introduced by the zero padding. Windowing with a Hann window was also tested, but eventually the boxcar window was selected as it retains the maximum spectral resolution, and it also gave lower error function values for the majority of the simulated fields. Analogous to parameter estimation with nonzero fields P_{avg} was constructed using a centered moving average of seven contiguous fields, and the 3 by 3 pixel area in the middle of the spectrum image was left out from the error function analysis.

Figure 6 presents an example of a simulated and windowed reflectivity field and the corresponding P_{avg} with estimated B_λ. The average values and 95% confidence intervals from 15 parameterization runs using simulated reflectivity fields are presented in Figure 7, and Figure 8 presents the scatterplots of estimated parameters against their expected values.

3.2.1. Sensitivity of GSI Parameter Estimates to *WAR*
The sensitivity of the GSI parameter estimates to varying degrees of intermittency was investigated by repeating the parameterization for the nonzero random fields using the boxcar window, and by parameterizing random fields with a gradually decreasing value of *WAR* from 1.0 to 0.1 in steps of 0.1. Fields with a
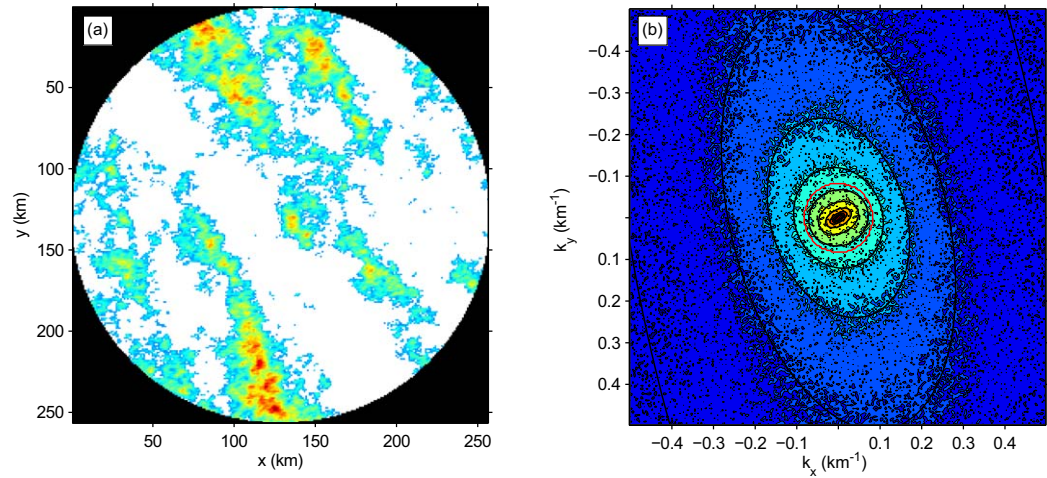
Figure 6. (a) An example of a simulated reflectivity field windowed with a boxcar window, generated with $\mathbf{G}=\mathbf{G}(-0.2,-0.2,0.2)$ and $l_s=$ 12 km. (b) P_{avg} corresponding to the real-space field on the left with selected B_λ (black ellipses) produced with estimated generator parameters $\mathbf{G}=\mathbf{G}(-0.171,-0.203,0.166)$ and $l_s=12.07$ km (red circle). If $\mathbf{G}$ and l_s are correct, B_λ should describe isolines on P_{avg}.

desired *WAR* value and without the wrap-around effect were created following the same procedure as in section 3.2 but excluding the final Step (6) of scaling and shifting the fields. Boxcar window was used in the parameterization of the fields, and for each case the average value of 15 parameterization runs was used as the estimator $\hat{\theta}_i$ of parameter θ_i for field i. To quantify the accuracy and the reliability of the parameter estimates throughout the entire time series, the mean absolute error (MAE) and the mean bias were calculated (Table 1):

$$MAE=\sum_{i=1}^{n}\frac{|\hat{\theta}_i-\theta_i|}{n} \quad (15)$$

$$bias=\sum_{i=1}^{n}\frac{\hat{\theta}_i-\theta_i}{n} \quad (16)$$

where n is the number of time steps in the time series. MAE and bias were calculated only for fields with $c > 0.1$ and/or $f > 0.1$ as parameters e and l_s are irrelevant in mildly anisotropic situations having therefore large variability in their estimates (see Discussion). Average values of c, e, f, and l_s for *WAR* values of 1.0, 0.5, and 0.1 are presented in Figure 9 together with the input values for each time step.

3.3. Measured Radar Reflectivity Fields

The studied rain event was captured by Mt. Stapylton radar near Brisbane, Australia, on 11 December 2010 from 00:00 UTC to 20:00 UTC. Instantaneous radar reflectivity values recorded at the interval of 6 min were processed into reflectivity (dBZ) fields having a resolution of 1 km and covering a 256 km by 256 km square centered at the radar. This event represents a very anisotropic storm that moves over the
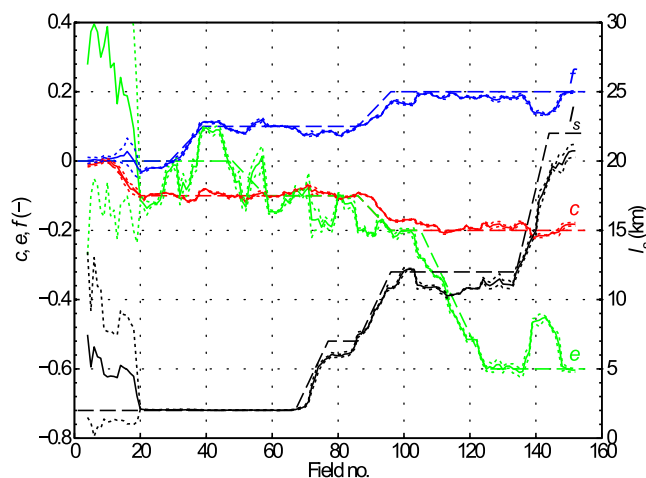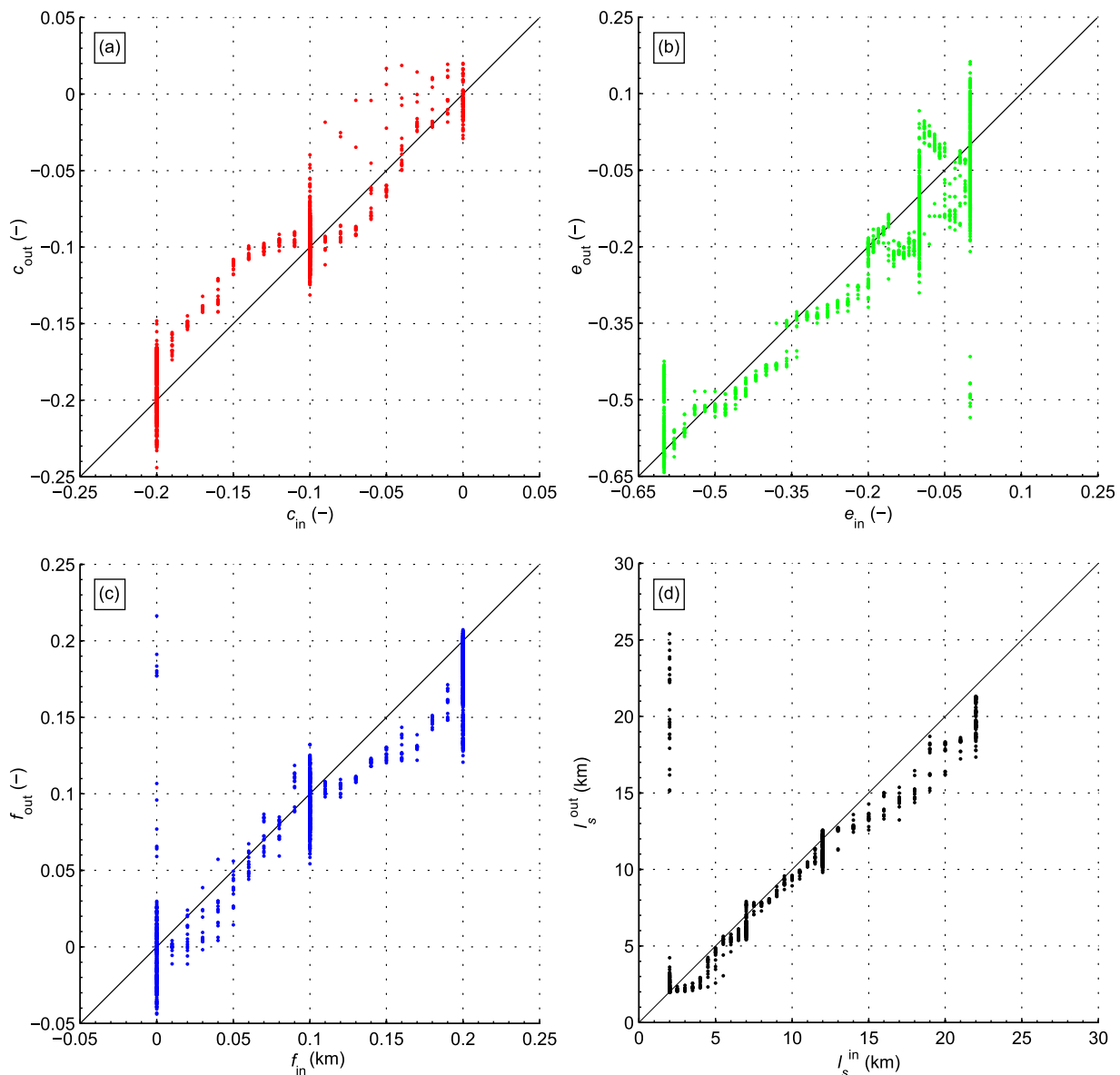

Figure 7. Average values (solid lines) and 95% confidence limits (dotted lines) of estimated anisotropy parameters for 15 parameterization rounds using simulated reflectivity fields (*WAR* = 0.38) with gradually changing anisotropy. Dashed lines indicate input parameters. *c*—red, *e*—green, *f*—blue, and l_s—black.

Figure 8. Relationship between input (horizontal axis) and estimated (vertical axis) anisotropy parameters for 15 parameterization rounds using simulated reflectivity fields. (a) c, (b) e, (c) f, and (d) l_s. Note that scale for e_{out} and l_s^{out} is truncated due to the large variance near $e_{in} = 0$ and $l_s^{in} = 2$ km.

radar from the north-west (NW) to the south-east (SE). Figure 10 presents the evolution of the storm throughout the event, and Figure 11 shows the time series of areal estimates of μ, σ, and *WAR* over the 256 by 256 km^2 square.

A centered moving average of 11 contiguous fields was used to produce P_{avg}, corresponding to an averaging time period of 60 min. Similar to the analysis of simulated reflectivity fields, a boxcar window was used prior to power spectrum estimation and the 3 by 3 pixel area in the middle of the spectrum image was neglected from computation of the error function.

As with simulated fields, the parameterization procedure was repeated 15 times to evaluate the reliability of the proposed method. The average parameter values and 95% confidence limits for each parameter and each time step are presented in Figure 12. One of the 15 parameterization rounds resulted in erroneous values of **G** and l_s for the time period between 00:00 and 04:00 UTC as revealed by much larger value of E^2 in comparison to the other 14 rounds. This affected the average value and increased the width of the

Table 1. Sensitivities of GSI Parameter Estimates to Varying Degrees of Intermittency[a]

	c		e		f		l_s	
	Bias	MAE	Bias	MAE	Bias	MAE	Bias	MAE
ideal	−0.003	0.004	−0.005	0.010	0.001	0.004	0.017	0.123
ideal$_{boxcar}$	0.006	0.009	−0.012	0.022	−0.008	0.009	−0.097	0.291
$WAR_{1.0}$	0.012	0.012	−0.009	0.033	−0.010	0.013	−0.119	0.419
$WAR_{0.9}$	0.010	0.013	−0.008	0.038	−0.012	0.015	−0.293	0.482
$WAR_{0.8}$	0.011	0.013	−0.008	0.038	−0.013	0.015	−0.185	0.433
$WAR_{0.7}$	0.010	0.013	−0.008	0.039	−0.014	0.016	−0.245	0.457
$WAR_{0.6}$	0.010	0.013	−0.006	0.040	−0.014	0.016	−0.353	0.493
$WAR_{0.5}$	0.008	0.011	−0.007	0.041	−0.015	0.017	−0.494	0.560
$WAR_{0.4}$	0.008	0.012	−0.012	0.048	−0.017	0.019	−0.628	0.676
$WAR_{0.3}$	0.006	0.013	−0.013	0.049	−0.015	0.016	−0.795	0.820
$WAR_{0.2}$	0.005	0.012	−0.014	0.062	−0.012	0.018	−0.830	0.848
$WAR_{0.1}$	−0.006	0.013	−0.019	0.068	−0.014	0.019	−1.032	1.059

[a]MAE, mean absolute error; ideal, nonzero random fields; ideal$_{boxcar}$, nonzero random fields with boxcar window; WAR_i, simulated fields with wetted area ratio i.

confidence intervals particularly for parameters e and l_s. In order to assess the effect of these erroneous parameter estimates, Figure 12 also presents the average values and 95% confidence intervals for parameters e and l_s for this time period without the erroneous values.
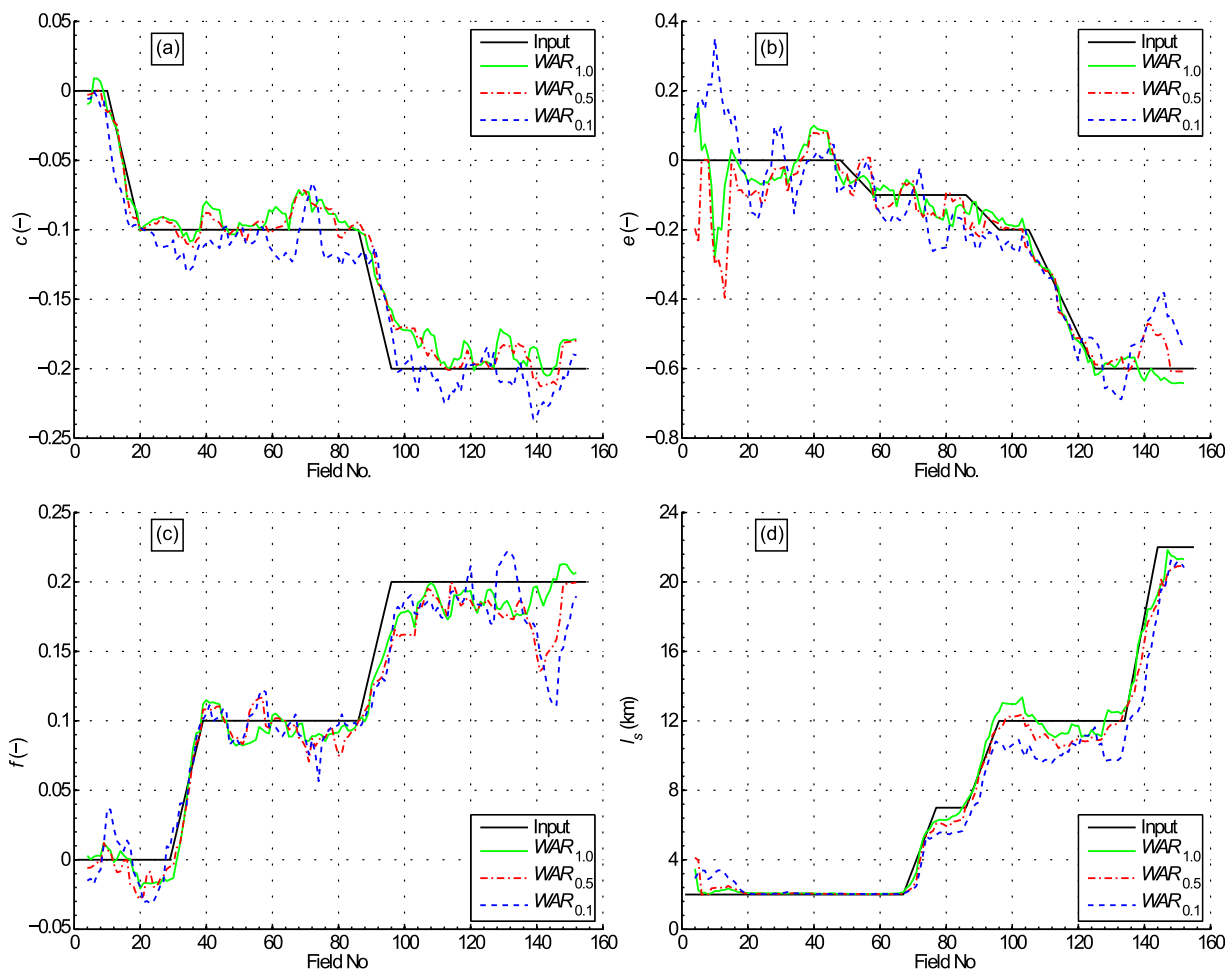

Figure 9. Average values of estimated anisotropy parameters for 15 parameterization rounds using random fields with WAR values of 1.0, 0.5, and 0.1. (a) c, (b) e, (c) f, and (d) l_s.
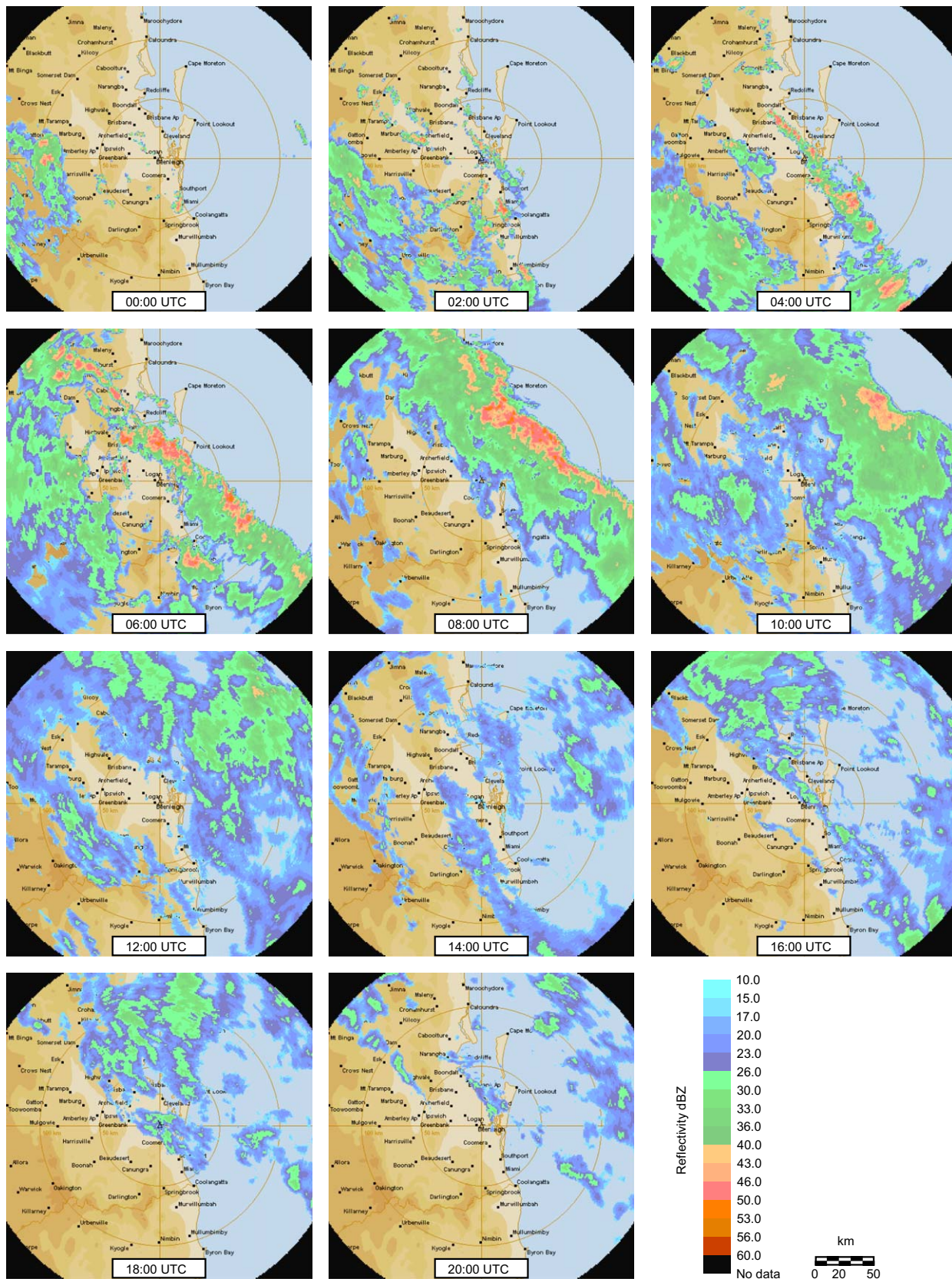
Figure 10. Measured radar reflectivities (dBZ) over a study area of 256 km by 256 km at Brisbane, Australia on 11 December 2010, at selected times. The spatial resolution is 1 km. The movement of the storm is from NW to SE direction.
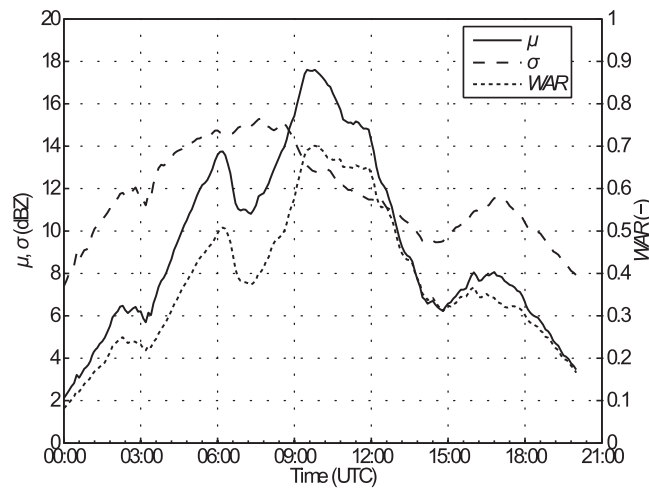
Figure 11. Spatial statistics for windowed measured reflectivity fields over the 256 km by 256 km study area. μ (dBZ; solid line), σ (dB; dashed line), and WAR (dotted line).

To give a better understanding of the effect of different parameter values, Figure 13 presents contours of P_{avg} near the largest scales with a few different B_λ computed using the estimated **G** and l_s at 07:00 UTC and at 14:30 UTC, representing two situations where the estimated parameters are relatively different. The reflectivity fields at these times are presented to relate the parameter values to the rainfall patterns. The reflectivity images are presented with a boxcar window to facilitate the interpretation of the images by showing only the region that was used in creating P_{avg}.

Finally, a measured reflectivity field at 07:00 UTC (Figure 13a) is compared to an isotropic and an anisotropic field generated using the method described in section 2.3 (Figure 14). Both fields were generated using the same random number generator seed and the same spatial statistics (μ=11.02 dBZ, σ=15.02 dB, WAR=0.38, and β=2.85) corresponding to the estimated statistics at 07:00 UTC. The anisotropic field was generated using the anisotropy parameters estimated from P_{avg} corresponding to the measured field; $\mathbf{G}=\mathbf{G}(-0.132,-0.364,0.038)$ and l_s=2.48 km.

4. Discussion

Under ideal conditions, i.e., using generated nonzero fields, the proposed method performed well finding all the parameters throughout the event with negligible bias and variance in the estimated parameters values (Figures 4 and 5). The only exception was parameter e in the beginning of the event when the fields being initially isotropic started gradually attain more anisotropic characteristics. When the field is fully isotropic ($c=f=0$), the parameters e and l_s, controlling the rotation of the system and the location of the sphero scale, respectively, completely lose their relevance. Consequently, any values of e and l_s should result in the same error function value. Here the fields are close to being isotropic (c and f are close to zero), which reduces the sensitivity of the error function to the values of e and l_s and is seen as wide confidence intervals for parameter e in Figure 4 for fields 0–20, and as a large spread in values of e_{out} when $-0.1 < e_{in} \leq 0$ in Figure 5b. The values of e and l_s were forced to 0 and 2 km, respectively, when the fields were close to isotropic, i.e., $|c| < 0.01$ and $|f| < 0.01$, as it is feasible to assume that the transformation from isotropic conditions to anisotropic conditions will be gradual, i.e., e and l_s will have small values in mildly
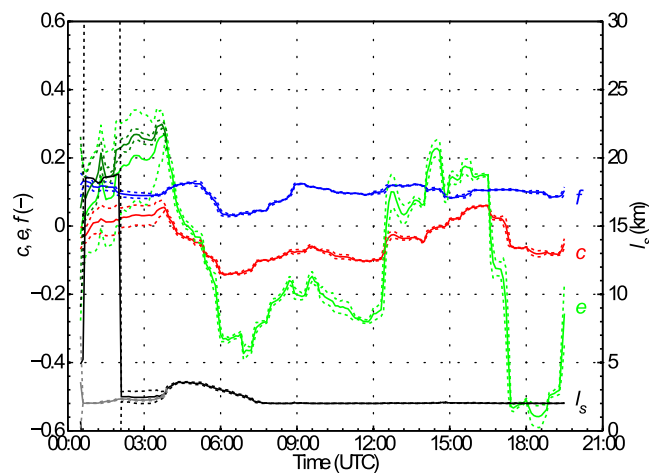

Figure 12. Average values (solid lines) and 95% confidence limits (dotted lines) of estimated anisotropy parameters for 15 parameterization rounds using measured radar reflectivity fields. c—red, e—green, f—blue, l_s—black, e without the erroneous values from one parameter estimation round is shown with dark green, and l_s without the erroneous values from the same round is shown with gray.
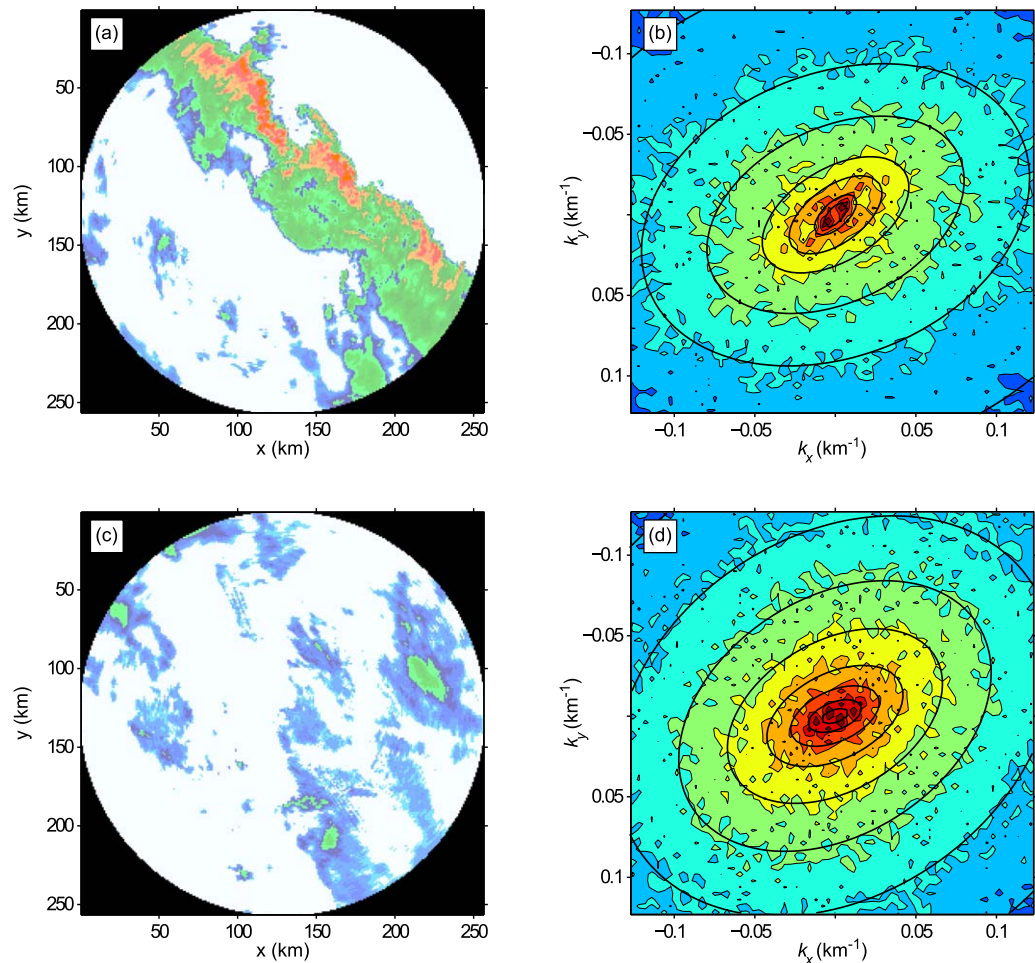
Figure 13. Measured reflectivity field windowed with a boxcar window (a) at 07:00 UTC and (c) at 14:30 UTC. (b) Contours of P_{avg} near the largest scales with selected B_λ (ellipses) corresponding to estimated $\mathbf{G}=\mathbf{G}(-0.132, -0.364, 0.038)$ and $l_s=2.48$ km at 07:00 UTC, and (d) $\mathbf{G}=\mathbf{G}(-0.004, 0.228, 0.101)$ and $l_s=2.04$ km at 14:30 UTC.

anisotropic conditions. The change from an isotropic to an anisotropic system is however challenging, as it can be seen from Figure 4 that e behaves well as long as the values of both $|c|$ and $|f|$ remain below 0.01, but as soon as $|c|$ starts to increase the variance in the estimated value of e is greatly enhanced until the system is anisotropic enough to restore the estimate of e back to the correct track.

The method was also capable of retrieving the original parameter values for simulated reflectivity fields where intermittency of rainfall is accounted for (Figure 7). However, there is a slight bias toward isotropy in parameters c, f, and l_s at the end of the event when the generated fields are most anisotropic. There is also a small increase in the variance of parameter values when compared to nonzero fields, as illustrated by the increased width in the scatterplot pattern of estimated parameters (see Figures 5 and 8). The main difference in estimated parameter values between nonzero fields and simulated reflectivity fields is the increased fluctuations around the original parameter values especially with parameter e (see Figures 4 and 7). These fluctuations together with the uneven distribution of input values are also causing the sudden increase in the spread of output values in Figures 5 and 8 when input parameters are held constant (e.g., for f_{in} values of 0, 0.1 and 0.2), as all the output values are being plotted against the same input value, but there are, e.g., 15×60 points with $f_{in}=0.2$ and only 15×1 points with $f_{in}=0.15$.

It seems that while the proposed method is able to find accurate estimates for the parameter values for nonzero fields, any change away from these ideal conditions will create perturbations to the power spectrum. These perturbations, in turn, are reflected in the estimated parameter values as small deviations from the values used in generating the fields. This is, however, not a defect of the parameterization method but
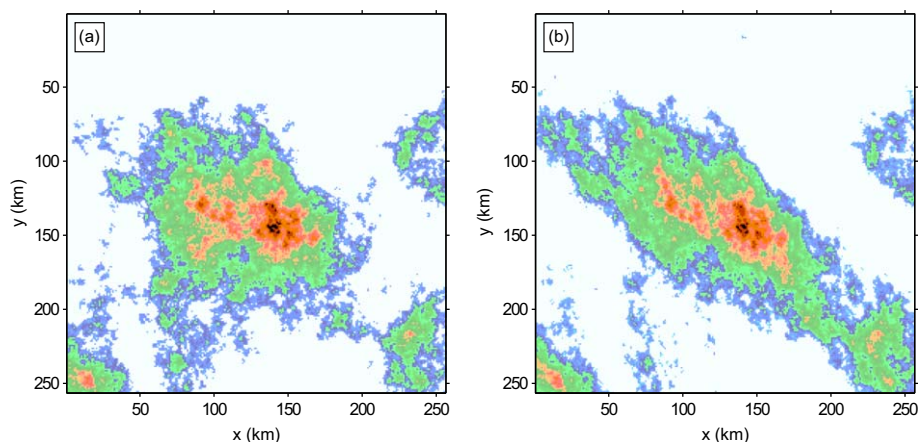
Figure 14. (a) An example of an isotropic field generated with estimated spatial statistics of the measured field in Figure 13a: μ=11.02 dBZ, σ=15.02 dB, WAR=0.38, and β=2.85. (b) Anisotropic field generated with the same spatial statistics and the same random generator seed as the isotropic field using estimated anisotropy parameters of Figure 13a: $\mathbf{G}=\mathbf{G}(-0.132, -0.364, 0.038)$ and l_s=2.48 km.

rather a consequence of the thresholding and windowing operations that alter the power spectra, as can be seen from the increased values of MAE for all the GSI parameters when the boxcar window is introduced to nonzero fields (Table 1). Perhaps surprisingly, the values of MAE are further increased when windowed nonzero fields (that wrap around the edges) are compared to windowed random fields with $WAR = 1.0$ (that do not wrap around the edges), indicating that the wrap-around effect is important also for windowed fields. This is a practical limitation of the method, as measured precipitation fields do not wrap around the image edges.

Thresholding (setting pixels with a value smaller than some threshold to zero) results in a significant loss of information in the image when compared to nonzero fields, explaining the increased MAE with decreasing WAR for parameters e, f, and l_s (Table 1). The bias toward isotropy in simulated reflectivity fields (Figure 7) for parameters c, f, and l_s is consistent with the overall bias for the parameters in Table 1. Even though the parameter estimates deteriorate with decreasing WAR, in practice the differences are small and even with WAR=0.1 the parameter estimates are of a relatively good accuracy (Figure 9). Consequently, while there clearly is a difference in the accuracy of retrieving known anisotropy parameters for generated nonzero fields ($WAR = 1$) and more realistic fields with $WAR < 1$, this difference can be attributed to the information content of the images.

As noted above for nonzero fields, parameters e and l_s become irrelevant for isotropic fields, and in the case of simulated reflectivity fields the estimated values for both these parameters have high variance in the beginning of the simulation when the fields are close to being isotropic (Figure 7). This is only of minor significance, though. The parameters c and f are estimated correctly also in near isotropic situations, and the values for e and l_s are estimated correctly once the fields become more anisotropic. Unlike with the nonzero fields, forcing the value of e to 0 and the value of l_s to 2 km when $|c| < 0.01$ and $|f| < 0.01$ was not successful here due to the reduced accuracy in the estimates of c and f. For operational use it would be beneficial to have a two-step parameterization process, where it is first determined whether the system is anisotropic enough to be parameterized and parameters are then estimated only for the anisotropic cases. This would also save computational burden by eliminating the need to estimate unnecessary parameters.

To assess whether the estimated parameter values for the measured radar reflectivity fields are acceptable, the visual appearance of the time series is analyzed first. The overall behavior of the time series for each of the estimated parameters is stable, i.e., the means of the estimated parameter values in Figure 12 do not fluctuate much. This indicates that the low-frequency variations are due to actual changes in the anisotropic structure of the fields while the small fluctuations are due to the noise in the spectrum estimates, which was the case with simulated reflectivity fields, too. Furthermore, at least parameters c and f can be related to visual observations. These are the parameters that control the stratification of the system in north-south and east-west (c) and diagonal (f) directions. Parameter f remained approximately constant throughout the event at around 0.1, which indicates contraction of structures larger than l_s in NE-SW direction. The

estimated l_s was found to lie at the smallest scales throughout the event, which is in accordance with previous observations [*Zawadzki*, 1973; *Kumar and Foufoula-Georgiou*, 1993b]. The resulting elongated large structures and isotropic small structures are in a good agreement with measured radar reflectivities shown in Figure 10. Parameter *c* on the other hand is mostly negative during the event, indicating further contraction of largest structures in the east-west direction. Also, there appears to be a positive correlation between parameters *c* and *e*. This may well be characteristic to the storm event studied here, rather than a universal phenomenon, but it would be worth to investigate this further by analyzing other storm events.

Although the studied event is very anisotropic, the anisotropy is changing only slightly during the event, which can be attributed to its short duration. Some differences can be distinguished, however, e.g., between 07:00 and 14:30 UTC (Figure 13). The orientation of the largest structures being different is depicted by B_λ at the very smallest frequencies having their major axis oriented slightly more in the NEE-SWW direction at 14:30 than at 07:00 when the corresponding B_λ are oriented more in the NE-SW direction. This corresponds to the largest structures being oriented more in NNW-SSE direction at 14:30 whereas at 07:00 the orientation is approximately in NW-SE direction. The effect of parameter *e* can be seen as the difference in the degree and the direction of rotation of B_λ between different scales in Figure 13. Although the change in the pair of spectra is small it is still detectable, and the method proposed here is capable of identifying the (small) changes in anisotropy. The capacity to automatically identify the changing anisotropy is valuable, particularly as over a longer period of time the anisotropy can change substantially.

The confidence intervals for the estimated parameters for both the simulated cases and the measured case are very narrow throughout the studied events and the optimal parameter values (not shown here) are constantly close to the estimated average values, apart from the isotropic and near isotropic situations in the simulated events (Figures 4 and 7) and the time period of 00:00–04:00 UTC of the measured event (Figure 12). Consequently, instead of running ensemble parameter estimations results from any single parameter estimation round could be used as estimated parameter values. Furthermore, these results imply that the downhill simplex algorithm is a suitable tool for finding the error function minimum. The wide confidence intervals between 00:00 and 04:00 UTC in the measured event (Figure 12) are due to the variability in parameter estimates during this period, indicating that downhill simplex had difficulties in finding the global optimum for these fields. This can be seen by removing the clearly erroneous estimates for *e* and l_s, which of course results in a considerable improvement in estimated values, but still leaves wider confidence intervals for the beginning of the event than for the later times.

Comparing the simulated isotropic and anisotropic fields (Figure 14) to the measured field (Figure 13a) confirms that there is a substantial difference between the simulated fields and that the isotropic simulation is not representative of the studied event with a distinct rainband. The anisotropic simulation on the other hand reproduces the orientation and overall elongation of the measured event well, demonstrating that anisotropy should be taken into account if more realistic looking fields are to be generated.

The method proposed here can be seen more as an image processing approach to quantify the anisotropy of geophysical fields than the more scaling oriented approaches of *Pflug et al*. [1993] and the SIG method of *Lewis et al*. [1999]. Here the scaling in the form of parameter β is not present in the anisotropy estimation itself but the approach simply identifies a spatial transformation from isotropic wavelengths to anisotropic wavelengths. This has the added benefit of reducing the number of parameters by one, since the scaling parameter is not estimated simultaneously as in the method of *Pflug et al*. [1993]. In SIG, the scaling is not estimated simultaneously with the GSI parameters, but it has to be estimated a priori using equation (3). In this regard, another major difference of the proposed method to earlier work is that here the parameterization can be run without user intervention by estimating the values of **G** and l_s directly using the error function E^2. In *Pflug et al*., [1993] and in SIG, a two-step procedure is required to estimate **G** and l_s separately. Because of this, the parameter space in SIG is only three dimensional, but the introduced extra effort from first estimating the scaling parameter, then **G** and only then l_s cancels out the extra benefit gained from a smaller parameter space. Furthermore, the proposed method is aimed to be used for quantifying the anisotropy of a time series of consecutive precipitation fields, instead of individual fields as in *Pflug et al*. [1993] or SIG. *Beaulieu et al*. [2007] on the other hand estimate the GSI parameters by visually examining scatterplots describing properties of isolines in $P(\boldsymbol{k})$, presenting a method that is easy to approach but laborious when estimating parameters of more than a few fields.

The computational burden of the proposed method could be reduced by decreasing the parameter space by setting values of e and l_s constant. For the measured event presented here, the sphero scale is near the smallest scales throughout the event and could be given a constant value of, say, 2 km prior to parameter estimation. Similarly, the rotation between structures of different sizes is minor in this case, and parameter e could be fixed to a value of zero for parameter estimation, forcing all the scales to have the same orientation of anisotropy. Having the possibility to identify all four parameters could, however, be essential in other occasions. *Ebtehaj and Foufoula-Georgiou* [2010] present a case where a storm event captured by a radar over the Appalachian Mountains in June 1995 had the small-scale features perpendicular to the mountain ridge, the intermediate scales isotropic, and the large-scale features parallel to the ridge line. Events like this highlight the parsimony of GSI-based methods to quantify the anisotropy across all scales using a single parameter set of generator **G** and sphero scale l_s. Alternatively, the anisotropy could be described using geostatistical methods, i.e., the nested variogram model of geometric anisotropy with one variogram describing small structures and another one describing large structures. Such a setup would, however, result in a larger number of parameters to be identified. Admittedly, especially in cases where there is no rotation between different scales the variogram method has the advantage of being more approachable having parameters that are easier to interpret than the GSI parameters.

The proposed method requires sufficient spatial and temporal resolutions of the input data in order to give adequate estimates of the prevailing anisotropy. Fine spatial resolution relative to size of the rain structures is required for capturing the rain patterns without too much distortion, whereas fine temporal resolution is necessary to include a sufficient number of fields for P_{avg} without the structure of the rain event changing considerably during the averaging period. Data for mesoscale events observed with the current generation of C and S-band radar networks and processed into Cartesian grid with spatial resolution of 1–2 km and temporal resolution of 5–10 min with domain sizes in the order of 100×100 to 300×300 km^2 are available in large quantities. These offer a solid basis for identifying anisotropy of storm events using the proposed method. If the domain size is considerably smaller than this both spatial and temporal resolutions of the data need to be increased to account for the rapid movement of the storm over the domain and for the small-scale changes in the storm structure. Large domain sizes on the other hand present the problem of increased intermittency and heterogeneity, as it is likely that there is rain only over a part of the domain or that the event changes its spatial structure within the domain. While the method was shown to perform relatively well in situations with high intermittency, the heterogeneity is problematic as the linear GSI assumes homogeneity over the study domain. The simplest solution to deal with heterogeneous situations is to divide the domain into smaller subregions and, assuming that the homogeneity assumption then holds, to estimate the anisotropy for each subregion separately. This requires, however, the data to have sufficient spatial and temporal resolutions to give adequate estimates for the GSI parameters. A better option would be to use the nonlinear GSI, but this would increase the complexity of the method as **G** would become a function of location. From a practical point of view, large domain sizes with high resolution may present a problem with increased computation time. However, using modern hardware with multiple CPU cores the process can be speeded up by parallelizing the computation of most time consuming parts of the process. While it is not required for the domain to be a square, it has the practical advantage of being easily windowed into a circle with the minimum loss of data. Even with windowing, misinterpreting the spatial structure of a storm due to the limited view of radar can pose a problem when a storm is entering or exiting the radar view. This can result in, e.g., an isotropic storm to appear as anisotropic when only the edge of the storm is visible for radar. The method furthermore assumes the power spectrum of rain fields to be approximated as a set of ellipses, and is not suited for situations that require a more complicated description of the scale geometry unless the number of parameters is increased.

5. Conclusions

Anisotropy of the precipitation fields plays a significant role in determining the catchment's response to a rainstorm, and should therefore be taken into account when generating stochastic rain events. In this paper, a new method, based on the linear GSI, to quantify the anisotropy of a time series of precipitation fields has been proposed. The proposed method was evaluated using nonzero random fields with a known anisotropy (ideal conditions), simulated radar reflectivity fields with a known anisotropy, and measured radar reflectivity fields with an unknown anisotropy.

Using nonzero random fields, the anisotropy parameters were retrieved accurately with negligible bias and variance. The accuracy of the parameter estimates is reduced slightly and fluctuations around the original (input) values are introduced when taking into account the intermittency in simulated reflectivity fields. The reduced accuracy in parameter estimates can be attributed to the lost information due to the introduced intermittency. In isotropic systems, GSI parameters e and l_s lose their relevance, which complicated their estimation in near-isotropic conditions. However, the parameters controlling whether the system is isotropic or anisotropic (c and f) are estimated accurately also in such conditions. Parameter estimates for measured reflectivity fields corresponded well with visual observations of the storm event. Even though the anisotropy does not change significantly during the event, the method was able to detect even the small changes in anisotropy.

The proposed method provides for quantification of anisotropy in geophysical fields an alternative that is easier to use and requires less user interaction and decision making than existing methods relying on GSI. Furthermore, the existing methods are intended to be used for individual fields, whereas the proposed method operates with a time series of fields. These are valuable aspects when dealing with precipitation events that typically comprise long time series of fields that are impractical to be handled individually or manually. In future, it would be interesting to compare the performance and the ease-of-use of the proposed method to the existing GSI-based and other methods. Furthermore, the proposed method should be tested using other, possibly more challenging case studies, to better evaluate its applicability as a tool for anisotropy quantification in precipitation fields.

References

Ali, A., T. Lebel, and A. Amani (2005), Rainfall estimation in the Sahel. Part I: Error function, *J. Appl. Meteorol.*, *44*(11), 1691–1706, doi:10.1175/JAM2304.1.

Baldwin, M. E., J. S. Kain, and S. Lakshmivarahan (2005), Development of an automated classification procedure for rainfall systems, *Mon. Weather Rev.*, *133*(4), 844–862, doi:10.1175/MWR2892.1.

Beaulieu, A., H. Gaonac'h, and S. Lovejoy (2007), Anisotropic scaling of remotely sensed drainage basins: The differential anisotropy scaling technique, *Nonlinear Processes Geophys.*, *14*(4), 337–350, doi:10.5194/npg-14-337-2007.

Bell, T. L. (1987), A space-time stochastic model of rainfall for satellite remote-sensing studies, *J. Geophys. Res.*, *92*(D8), 9631–9643, doi:10.1029/JD092iD08p09631.

Berne, A., G. Delrieu, and B. Boudevillain (2009), Variability of the spatial structure of intense Mediterranean precipitation, *Adv. Water Resour.*, *32*(7), 1031–1042, doi:10.1016/j.advwatres.2008.11.008.

Brauer, C. C., A. J. Teuling, A. Overeem, Y. van der Velde, P. Hazenberg, P. M. M. Warmerdam, and R. Uijlenhoet (2011), Anatomy of extraordinary rainfall and flash flood in a Dutch lowland catchment, *Hydrol. Earth Syst. Sci.*, *15*(6), 1991–2005, doi:10.5194/hess-15-1991-2011.

De Michele, C., and P. Bernardara (2005), Spectral analysis and modeling of space-time rainfall fields, *Atmos. Res.*, *77*(1–4), 124–136, doi:10.1016/j.atmosres.2004.10.031.

Doswell, C. A., H. E. Brooks, and R. A. Maddox (1996), Flash flood forecasting: An ingredients-based methodology, *Weather Forecasting*, *11*(4), 560–581, doi:10.1175/1520-0434(1996)011<0560:FFFAIB>2.0.CO;2.

Ebtehaj, M., and E. Foufoula-Georgiou (2010), Orographic signature on multiscale statistics of extreme rainfall: A storm-scale study, *J. Geophys. Res.*, *115*, D23112, doi:10.1029/2010JD014093.

Ebtehaj, M., and E. Foufoula-Georgiou (2011), Statistics of precipitation reflectivity images and cascade of Gaussian-scale mixtures in the wavelet domain: A formalism for reproducing extremes and coherent multiscale structures, *J. Geophys. Res.*, *116*, D14110, doi:10.1029/2010JD015177.

Fox, C. G., and D. E. Hayes (1985), Quantitative methods for analyzing the roughness of the seafloor, *Rev. Geophys.*, *23*(1), 1–48, doi:10.1029/RG023i001p00001.

Germann, U., and I. Zawadzki (2002), Scale-dependence of the predictability of precipitation from continental radar images. Part I: Description of the methodology, *Mon. Weather Rev.*, *130*(12), 2859–2873, doi:10.1175/1520-0493(2002)130<2859:SDOTPO>2.0.CO;2.

Gires, A., C. Onof, C. Maksimovic, D. Schertzer, I. Tchiguirinskaia, and N. Simoes (2012), Quantifying the impact of small scale unmeasured rainfall variability on urban runoff through multifractal downscaling: A case study, *J. Hydrol.*, *442-443*, 117–128, doi:10.1016/j.jhydrol.2012.04.005.

Gupta, V. K., and E. C. Waymire (1993), A statistical analysis of mesoscale rainfall as a random cascade, *J. Appl. Meteorol.*, *32*(2), 251–267, doi:10.1175/1520-0450(1993)032<0251:ASAOMR>2.0.CO;2.

Houze, R. A., and P. V. Hobbs (1982), Organization and structure of precipitating cloud systems, *Adv. Geophys.*, *24*, 225–315, doi:10.1016/S0065-2687(08)60521-X.

Kang, B., and J. A. Ramírez (2010), A coupled stochastic space-time intermittent random cascade model for rainfall downscaling, *Water Resour. Res.*, *46*, W10534, doi:10.1029/2008WR007692.

Kirstetter, P.-E., G. Delrieu, B. Boudevillain, and C. Obled (2010), Toward an error model for radar quantitative precipitation estimation in the Cévennes–Vivarais region, France, *J. Hydrol.*, *394*(1-2), 28–41, doi:10.1016/j.jhydrol.2010.01.009.

Kumar, P. (1995), A wavelet based methodology for scale-space anisotropic analysis, *Geophys. Res. Lett.*, *22*(20), 2777–2780, doi:10.1029/95GL02934.

Kumar, P., and E. Foufoula-Georgiou (1993a), A multicomponent decomposition of spatial rainfall fields: 1. Segregation of large- and small-scale features using wavelet transforms, *Water Resour. Res.*, *29*(8), 2515–2532, doi:10.1029/93WR00548.

Kumar, P., and E. Foufoula-Georgiou (1993b), A new look at rainfall fluctuations and scaling properties of spatial rainfall using orthogonal wavelets, *J. Appl. Meteorol.*, *32*(2), 209–222, doi:10.1175/1520-0450(1993)032<0209:ANLARF>2.0.CO;2.

Leblois, E., and J.-D. Creutin (2013), Space-time simulation of intermittent rainfall with prescribed advection field: Adaptation of the turning band method, *Water Resour. Res.*, 49, 3375–3387, doi:10.1002/wrcr.20190.

Lewis, G. (1993), The scale invariant generator technique and scaling anisotropy in geophysics, MS thesis, Dep. of Phys., McGill Univ., Montreal, Que., Canada.

Lewis, G. M., S. Lovejoy, D. Schertzer, and S. Pecknold (1999), The scale invariant generator technique for quantifying anisotropic scale invariance, *Comput. Geosci.*, 25(9), 963–978, doi:10.1016/S0098-3004(99)00061-8.

Lovejoy, S., and D. Schertzer (1985), Generalized scale invariance in the atmosphere and fractal models of rain, *Water Resour. Res.*, 21(8), 1233–1250, doi:10.1029/WR021i008p01233.

Mandapaka, P. V., and X. Qin (2013), Analysis and characterization of probability distribution and small-scale spatial variability of rainfall in Singapore using a dense gauge network, *J. Appl. Meteorol. Climatol.*, 52(12), 2781–2796, doi:10.1175/JAMC-D-13-0115.1.

Mandapaka, P. V., P. Lewandowski, W. E. Eichinger, and W. F. Krajewski (2009), Multiscaling analysis of high resolution space-time lidar-rainfall, *Nonlinear Processes Geophys.*, 16(5), 579–586, doi:10.5194/npg-16-579-2009.

Marshall, J. S., and W. M. K. Palmer (1948), The distribution of raindrops with size, *J. Meteorol.*, 5(4), 165–166, doi:10.1175/1520-0469(1948)005<0165:TDORWS>2.0.CO;2.

Menabde, M., D. Harris, A. Seed, G. Austin, and D. Stow (1997), Multiscaling properties of rainfall and bounded random cascades, *Water Resour. Res.*, 33(12), 2823–2830, doi:10.1029/97WR02006.

Miniscloux, F., J. D. Creutin, and S. Anquetin (2001), Geostatistical analysis of orographic rainbands, *J. Appl. Meteorol.*, 40(11), 1835–1854, doi:10.1175/1520-0450(2001)040<1835:GAOOR>2.0.CO;2.

Nelder, J. A., and R. Mead (1965), A simplex method for function minimization, *Comput. J.*, 7(4), 308–313, doi:10.1093/comjnl/7.4.308.

Nykanen, D. K., and D. Harris (2003), Orographic influences on the multiscale statistical properties of precipitation, *J. Geophys. Res.*, 108(D8), 8381, doi:10.1029/2001JD001518.

Paschalis, A., P. Molnar, S. Fatichi, and P. Burlando (2013), A stochastic model for high-resolution space-time precipitation simulation, *Water Resour. Res.*, 49, 8400–8417, doi:10.1002/2013WR014437.

Pecknold, S., S. Lovejoy, D. Schertzer, C. Hooge, and J. F. Malouin (1993), The simulation of universal multifractals, in *Cellular Automata: Prospects in Astrophysical Applications*, edited by J. M. Perdang and A. Lejeune, pp. 228–267, World Sci., Singapore.

Pegram, G. G. S., and A. N. Clothier (2001), High resolution space–time modelling of rainfall: the "String of Beads" model, *J. Hydrol.*, 241(1–2), 26–41, doi:10.1016/S0022-1694(00)00373-5.

Pflug, K., S. Lovejoy, and D. Schertzer (1993), Differential rotation and cloud texture: Analysis using generalized scale invariance, *J. Atmos. Sci.*, 50(4), 538–554, doi:10.1175/1520-0469(1993)050<0538:DRACTA>2.0.CO;2.

Pilkington, M., and J. P. Todoeschuck (1993), Fractal magnetization of continental crust, *Geophys. Res. Lett.*, 20(7), 627–630, doi:10.1029/92GL03009.

Press, W. H., S. A. Teukolsky, W. T. Vetterling, and B. P. Flannery (2007), *Numerical Recipes: The Art of Scientific Computing*, 3rd ed., Cambridge Univ. Press, New York.

Radhakrishna, B., I. Zawadzki, and F. Fabry (2012), Predictability of precipitation from continental radar images. Part V: Growth and decay, *J. Atmos. Sci.*, 69(11), 3336–3349, doi:10.1175/JAS-D-12-029.1.

Rauber, R. M., and M. K. Ramamurthy (2003), MESOSCALE METEOROLOGY | Cloud and precipitation bands, in *Encyclopedia of Atmospheric Sciences*, edited by J. R. Holton, J. A. Pyle, and J. A. Curry, pp. 1243–1250, Academic, Oxford, U. K.

Rebora, N., L. Ferraris, J. von Hardenberg, and A. Provenzale (2006), RainFARM: Rainfall downscaling by a filtered autoregressive model, *J. Hydrometeorol.*, 7(4), 724–738, doi:10.1175/JHM517.1.

Rysman, J.-F., S. Verrier, Y. Lemaître, and E. Moreau (2013), Space-time variability of the rainfall over the western Mediterranean region: A statistical analysis, *J. Geophys. Res. Atmos.*, 118, 8448–8459, doi:10.1002/jgrd.50656.

Schertzer, D., and S. Lovejoy (1985), Generalised scale invariance in turbulent phenomena, *PhysicoChem. Hydrodyn.*, 6(5-6), 623–635.

Schertzer, D., and S. Lovejoy (1987), Physical modeling and analysis of rain and clouds by anisotropic scaling multiplicative processes, *J. Geophys. Res.*, 92(D8), 9693–9714, doi:10.1029/JD092iD08p09693.

Schleiss, M., J. Jaffrain, and A. Berne (2012), Stochastic simulation of intermittent DSD fields in time, *J. Hydrometeorol.*, 13(2), 621–637, doi:10.1175/JHM-D-11-018.1.

Schleiss, M., S. Chamoun, and A. Berne (2014), Stochastic simulation of intermittent rainfall using the concept of "dry drift," *Water Resour. Res.*, 50, 2329–2349, doi:10.1002/2013WR014641.

Schleiss, M. A., A. Berne, and R. Uijlenhoet (2009), Geostatistical simulation of two-dimensional fields of raindrop size distributions at the meso-γ scale, *Water Resour. Res.*, 45, W07415, doi:10.1029/2008WR007545.

Seed, A. W., R. Srikanthan, and M. Menabde (1999), A space and time model for design storm rainfall, *J. Geophys. Res.*, 104(D24), 31,623–31,630, doi:10.1029/1999JD900767.

Seed, A. W., R. Srikanthan, and B. F. Taylor (2002), Stochastic space-time rainfall for designing urban drainage systems, paper presented at the International Conference on Urban Hydrology for the 21st Century, Department of Irrigation and Drainage, Kuala Lumpur, Malaysia.

Seed, A. W., C. E. Pierce, and K. Norman (2013), Formulation and evaluation of a scale decomposition-based stochastic precipitation nowcast scheme, *Water Resour. Res.*, 49, 6624–6641, doi:10.1002/wrcr.20536.

Segond, M.-L., H. S. Wheater, and C. Onof (2007), The significance of spatial rainfall representation for flood runoff estimation: A numerical evaluation based on the Lee catchment, UK, *J. Hydrol.*, 347(1–2), 116–131, doi:10.1016/j.jhydrol.2007.09.040.

VanZandt, T. E., S. A. Smith, T. Tsuda, T. Sato, S. Fukao, S. Kato, and D. C. Fritts (1990), Studies of velocity fluctuations in the lower atmosphere using the MU radar. Part I: Azimuthal anisotropy, *J. Atmos. Sci.*, 47(1), 39–50, doi:10.1175/1520-0469(1990)047<0039:SOVFIT>2.0.CO;2.

Velasco-Forero, C. A., D. Sempere-Torres, E. F. Cassiraga, and J. Jaime Gómez-Hernández (2009), A non-parametric automatic blending methodology to estimate rainfall fields from rain gauge and radar data, *Adv. Water Resour.*, 32(7), 986–1002, doi:10.1016/j.advwatres.2008.10.004.

Vischel, T., T. Lebel, S. Massuel, and B. Cappelaere (2009), Conditional simulation schemes of rain fields and their application to rainfall–runoff modeling studies in the Sahel, *J. Hydrol.*, 375(1–2), 273–286, doi:10.1016/j.jhydrol.2009.02.028.

Zawadzki, I. I. (1973), Statistical properties of precipitation patterns, *J. Appl. Meteorol.*, 12(3), 459–472, doi:10.1175/1520-0450(1973)012<0459:SPOPP>2.0.CO;2.